

Performance Evaluation and Improvement of Shoreline Detection Using Sentinel-1 SAR and DEM Data

Lena Chang[✉], Member, IEEE, and Yi-Ting Chen[✉]

Abstract—This study improved the shoreline detection performance based on the U-Net model by combining Sentinel-1 synthetic aperture radar (SAR) and digital elevation model (DEM) data. The U-Net network was first modified to enhance feature extraction by using the MobileNetV3 backbone architecture and convolutional block attention module. To alleviate the performance degradation of shoreline detection caused by radar shadow, especially in coastal areas with large terrain undulations, SAR and DEM data were combined as input to U-Net. Furthermore, this study evaluated the shoreline detection performance using the statistical analysis based on the proposed probabilistic model of distance difference between the detected shoreline and reference data which was provided by Construction and Planning Agency Ministry of the Interior, Taiwan government. The experiment was conducted based on two self-built datasets, one containing 4061 SAR images and the other containing 3822 SAR images and corresponding DEM data, both collected in the coastal areas of Taiwan from 2016 to 2019. The experimental results showed that compared with the U-Net network using SAR data, the modified U-Net has achieved superior performance in shoreline detection for various coastal landforms. Moreover, the addition of DEM data reduced the influence of radar shadow, making shoreline detection results more consistent with reference data. Finally, the generalization ability of the modified U-Net in shoreline detection was also verified by testing images from regions not included in the built dataset.

Index Terms—Digital elevation model (DEM), performance evaluation, Sentinel-1, shoreline detection, U-Net.

I. INTRODUCTION

THE shoreline is the continuous boundary between the ocean and the land, and is one of the important line features on the earth's surface. The coastal areas are rich in natural and biological resources, which are highly dynamic and diverse. These regions are crucial for maritime management, agriculture, ecosystems, human settlement, and approximately 60% of the

world's population lives within 150 km of the coastal zone [1]. Therefore, it is important to monitor the spatial and temporal changes of shorelines for sustainable coastal zone management and environmental protection.

Especially in Taiwan, a small island with a large population and rapid development, land space has always been in short supply. Most of the fishery resources come from coastal areas, which are also the main places for human economic activities. Coastline changes are not only affected by natural factors, but also by human activities. It is reported that the coastal area is vulnerable to tsunami, soil salinization, land subsidence, and sea water inundation [2]. Human destruction and improper development have caused serious damage to Taiwan's coast and sea areas. In addition, the diversity and complexity of coastal landforms increase the difficulty of shoreline detection. Therefore, it is a challenging and important task to accurately and effectively delineate the shoreline of Taiwan.

The shoreline detection by in situ measurements based on the global navigation satellite system (GNSS) is the traditional approach. Although the traditional method of the shoreline detection is accurate and detailed, it is long-term, laborious, and time consuming. Therefore, it is difficult to conduct in wide area [3]. Recently, the remote sensing data have become one of the preferred sources for shoreline detection due to its earth observation capability. Compared with the traditional methods, shoreline detection based on the satellite data has the advantages of low labor intensity, short time consumption, less equipment, and wide spatial coverage [4]. Optical remote sensing data provide an effective and fast method for detecting shorelines because of its imaging characteristics that conform to human visual interpretation [5]. Zhang et al. [6] proposed an automated method, object-based region growing integrating edge detection, which can accurately extract aquaculture coastlines from remotely sensed imagery with fine-to-moderate spatial resolution, providing an effective and cost-efficient solution for mapping complex coastal zones with human activities. Gens [7] provided a comprehensive review of the current status and maturity of remote sensing techniques for coastline detection, extraction, and monitoring, highlighting the shift from visual interpretation to advanced remote sensing methods in operational settings. Pardo-Pascual [8] evaluated the accuracy of shoreline positions obtained from infrared bands of Landsat-7, Landsat-8, and Sentinel-2 imagery on natural beaches, comparing them

Manuscript received 30 January 2024; accepted 3 April 2024. Date of publication 8 April 2024; date of current version 17 April 2024. This work was supported in part by the Ministry of Science and Technology, Taiwan, under Grant MOST 111-2119-M-019-003, and in part by the National Science and Technology Council, Taiwan, under Grant NSTC 112-2119-M-019-007. (Corresponding author: Lena Chang.)

Lena Chang is with the Department of Communication, Navigation and Control Engineering, National Taiwan Ocean University, Keelung 202301, Taiwan (e-mail: lenachang@mail.ntou.edu.tw).

Yi-Ting Chen is with the Department of Electrical Engineering, National Taiwan Ocean University, Keelung 202301, Taiwan (e-mail: 20953003@mail.ntou.edu.tw).

Digital Object Identifier 10.1109/JSTARS.2024.3385778

with high-precision shorelines from GNSS surveys and photogrammetry, and finding that short wave infrared bands are more reliable than near infrared bands for shoreline extraction. However, their practical applications are limited by the climate and illumination, as the weather in the coastal areas is often rainy, cloudy, and foggy, such as the study area of Taiwan. Whereas synthetic aperture radar (SAR) data have more advantages in the ability to monitor the shoreline even in bad weather conditions [9]. Therefore, SAR data have been proved to be an effective tool for shoreline detection because of its wide coverage, penetration and all day/weather imaging observations [10]. In recent years, there have been several studies on shoreline detection using SAR data, such as TerraSAR-X, RADARSAT, Cosmo-SkyMed and Sentinel. Modava et al. [11] proposed a novel algorithm for shoreline detection based on the local spectral histogram and the level set method by using TerraSAR-X and RADARSAT-2 data. Liu et al. [12] used the TerraSAR-X and RADARSAT-2 data to delineate the shoreline by combining the edge-based and region-based active contour models. Acar et al. [13] proposed an algorithm for automatic shoreline extraction from L-band PALSAR images. Wu et al. [14] investigated overall characteristics of ALOS-2 and Cosmo-SkyMed data around the shoreline especially focusing on clarification of the preferred observation conditions of L-band SAR for shoreline detection. Moreover, Mazzolini et al. [15] introduced an iterative method to delineate the shoreline from Sentinel-1 VH polarization data based on superpixel segmentation. Din et al. [16] analyzed two shoreline extraction methods using dual-polarization Cosmo-SkyMed data. Yu et al. [17] proposed a semi-automatic coastline extraction method based on region segmentation and edge detection for Landsat-5 data. Moreover, the numerical models are also used to detect the shoreline to assess both short-term and long-term shoreline temporal evolution. Spinosa et al. [18] used one threshold value to defined the profile of the detected edge and validated the results by comparing the average offset and root mean square error with in-situ measurements. Francone and Simmonds [19] verified the reliability of the general shoreline beach numerical model in predicting shoreline evolution, showing its accuracy in capturing day-to-day changes caused by wave attack on mixed beaches, and offering valuable insights for coastal morphodynamics research and management of coastal hazards.

Recently, convolutional neural networks (CNNs) and deep learning methods have been widely used in various fields of computer vision, such as segmentation, classification, and object detection. Especially for the fully convolutional networks, the semantic features extracted by the deep CNNs enable the entire network to complete the classification and prediction for each pixel while preserving the image information. U-Net [20] is a convolutional neural network developed for biomedical image segmentation. The U-Net is a fast and accurate pixel-based image segmentation method with a unique U-shaped structure consisting of encoder and decoder blocks. Zhang et al. [21] developed an automated method for accurate waterline extraction from SAR data based on the U-Net. The approach showed high accuracy and efficiency for shoreline detection in complicated large-scale tidal flats of study area, with precision

and recall being 0.8 and 0.9, respectively. Another study [22] proposed a CNN method using attention U-Net and a multiscale level set method to delineate the edge of the water body faster and more precisely from Gaofen-3 SAR data. Zhou et al. [23] demonstrated the application of DNN technology in waterline monitoring of SAR images through the modified U-Net network. The detection performance of the modified U-Net achieved over 98% F1-score in the task of sea-land segmentation.

However, it is well known that geometric distortion is an inherent error in SAR data due to topographic relief and side-looking geometry [24]. The existence of geometric distortion brings many negative effects, such as shadow, layover, and foreshortening on SAR images in mountainous areas. Therefore, the elevation information from digital elevation model (DEM) is necessary when the land areas affected by geometric distortion exhibit low backscatter values. Baumhoer et al. [25] introduced a modified U-Net for automatic extraction of Antarctic shorelines on dual-pol Sentinel-1 data and the Antarctic TanDEM-X DEM data. The deviations of the extracted shorelines in training and testing areas were 78 and 108 m on average, respectively. Heidler et al. [26] combined the semantic segmentation network U-Net and edge detection network holistically nested (HED) for coastline detection. The advantages of the HED-UNet model for simultaneous segmentation and edge detection were demonstrated on a dataset of Sentinel-1 and achieved over 92.9% detection accuracy.

In this study, a modified semantic segmentation U-Net network was proposed to detect the shoreline for the study area of Taiwan using the multitemporal SAR data provided by Sentinel-1. The U-Net model was modified by using the MobileNetV3 [27] backbone architecture and convolutional block attention module (CBAM) [28] to improve the feature extraction ability. Our previous study [29] showed that the geometric distortion of SAR data affected the shoreline detection performance in some regions with large slope fluctuations, especially the faulted coast in eastern Taiwan. To reduce the misclassification of these undulating regions, this study improved shoreline detection results by combining Sentinel-1 and DEM data. In addition, this study proposed a new edge evaluation metric to verify the performance of the modified U-Net in shoreline detection.

The rest of this article is organized as follows. Section II described the self-built dataset. The modified U-Net network and the performance evaluation metrics were introduced in Section III. Sections IV and V presented the experimental results and discussion, followed by the conclusion in Section VI.

II. MATERIALS

A. Study Area and Reference Data

In the study, the shoreline detection was conducted in the coastal area of the main island of Taiwan. The study area is located between the southeastern coast of the Asian continent and the East Asian islands distributed in the western Pacific Ocean, between 120°58'E to 122°06'E and 21°53'N to 26°23'N. The island of Taiwan is geologically active, formed on a complex convergent boundary between the Eurasian plate and the Philippine Sea plate. As shown in Fig. 1, in the northeast of

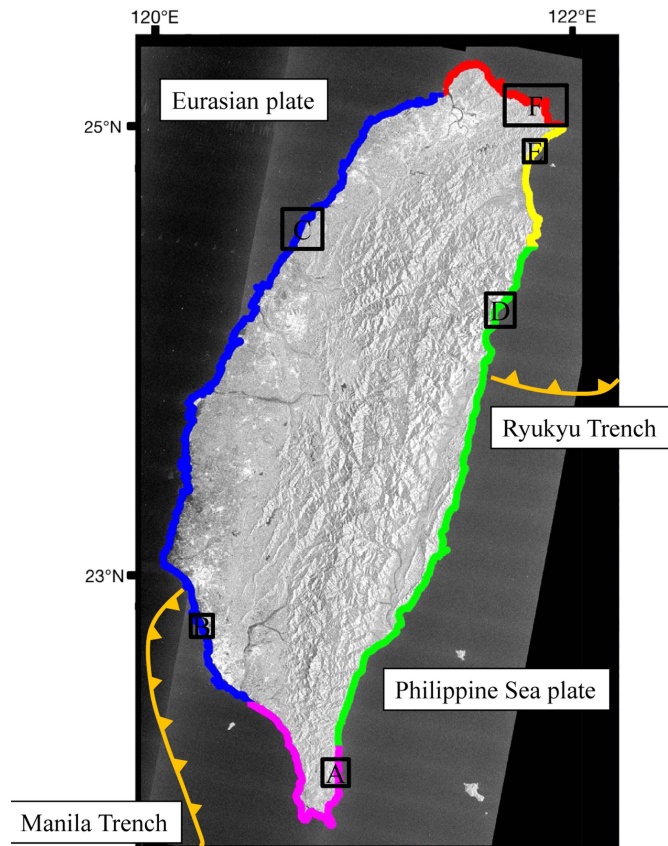


Fig. 1. Study area is the main island of Taiwan. Northern coast is the headland bay in red color. Northeast is a sandy coast in yellow color. Fault coast in the eastern with green color. Coral reefs coast in the southern with pink color. The west coast is sandy in blue color. The plate boundaries are shown in orange. The triangle represents the subduction direction of the plate. A–F are the six test regions selected from the study area.

Taiwan, the western edge of the Philippine Sea plate subducts below the Eurasian plate along the Ryukyu Trench. In the south of Taiwan, the subduction direction of the plate is opposite, and the Eurasian plate subducts eastward to the Philippine Sea plate along the Manila Trench. The island is about 395 km long and 144 km wide, with a total land area of about 36 000 square kilometers. The coastline of Taiwan's main island is about 1200 km long. Taiwan is one of the islands with the highest density of mountains in the world. Within an area of 36 000 square kilometers, there are 268 mountains about 3000 m above sea level. The undulating topography of the island leads to complex coastal terrain. The shorelines of Taiwan have different types of landforms, including the fault coast in the east, the sandy coast in the west and northeast, the headland bay in the north and the coral reef coast in the south, as shown in Fig. 1.

In order to develop a suitable shoreline detection algorithm, the coastal landform of the study area needs to be considered. Therefore, it is imperative to establish a dataset containing different types of coastal landforms to develop the proposed shoreline detection method. According to our previous study [29], the labeling of the dataset was done by the Otsu's thresholding method, morphological processing and assisted by the human inspection. The Sentinel-1 images were first binarized by

TABLE I
COMPLETE ACQUISITION DATES OF SENTINEL-1 DATA

Acquisition Dates	Orbit Modes	Ascending Orbit Mode	Descending Orbit Mode
2016		01/09, 09/17, 10/23, 11/16	06/3, 12/12
2017		04/21, 08/31, 09/24, 10/06	06/22, 08/21, 09/14, 10/20
2018		04/16, 07/21, 08/20, 09/07	07/11, 10/15, 12/02
2019		01/05, 08/09, 10/08, 11/25	01/15, 07/30, 09/04, 09/28
2020		11/01, 11/19	10/16

Otsu's thresholding method and the small textures and fragments in image segmentation results were removed through closing, opening, and hole filling operations of morphological processing. Moreover, the Construction and Planning Agency Ministry of the Interior (CPAMI) manually delineated the shoreline with relative high tide of the Taiwan twice a year. First, the investigators used GPS devices to record the location of the shoreline by ground survey at the scheduled pass time of satellite. Afterward, the shoreline mapping was manually delineated according to the GPS records. In addition, the shoreline maps representing reference data were further validated with high-resolution satellites (including FormoSat-5, SPOT-6/SPOT-7, QuickBird, and IKONOS) and aerial photographs. In the following experiments, the shoreline detection results were compared with the reference data provided by CPAMI.

B. Sentinel-1 Data and Preprocessing

Sentinel-1 is a constellation of two radar satellites, Sentinel-1A and Sentinel-1B, operated by the European Space Agency (ESA) with the first launched in 2014 and the second in 2016. The mission of Sentinel-1 satellites provides an independent operational capability for continuous radar mapping of the Earth with enhanced revisit frequency (12 days), wide coverage, reliability, and timelines for operational services and applications requiring long duration sequences. The Sentinel-1 satellite operates at the C-band with a central frequency 5.404 GHz, including VV and VH polarization data and the spatial resolution is 5 m \times 20 m in the range and azimuth directions. In this study, shoreline detection was performed using Sentinel-1 data in interferometric wide swath mode with 250 km swath width and Level-1 ground range detection format with 10 m \times 10 m pixel spacing. In addition, the incidence angles of the ascending and descending orbital modes in the study area are from 31.5° to 36.3° and 31.8° to 36.5°, respectively. In the study, Sentinel-1 data were collected from 2016 to 2020. The complete acquisition dates of Sentinel-1 data were shown in Table I.

The acquired SAR data were preprocessed using the sentinel application platform (SNAP) Sentinel-1 Toolbox software developed by ESA. Preprocessing includes four main steps. First, the orbit file was applied to update the Sentinel-1 data. Next, the pixel data were converted to an actual backscattering σ^0 in decibel (dB), also known as sigma naught, by using the radiometric calibration. Therefore, the pixel values can be directly related to the radar backscatter of the scene in the imagery. Then, a geometric calibration process was performed to remove topographical effects and the extents were projected to Taiwan Datum 1997 (TWD97) earth ellipsoid model. In addition, the DEM data corresponding to the SAR imagery was collected by

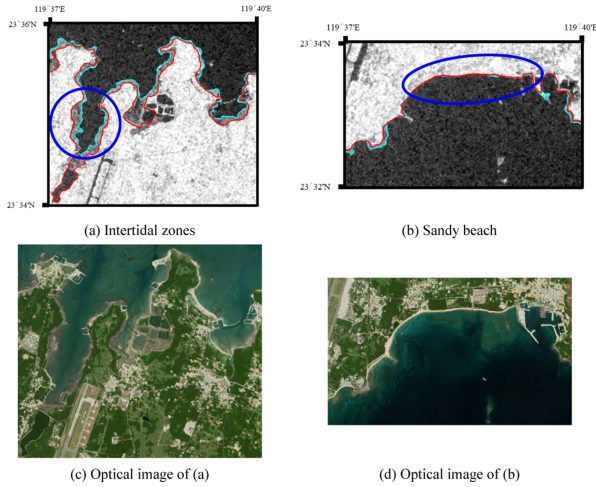


Fig. 2. Shoreline detection results of high and low tide levels. The cyan and red borders represent the detection results of low and high tide levels, respectively. The sampling date of high-tide image is August 31, 2022 with 90 cm tide level. The sampling date of low-tide image is August 7, 2022 with -83 cm tide level. (a) and (b) are images of low tide level.

SNAP during the terrain correction process, and the resolution of DEM has been adjusted to be the same as Sentinel-1 through the bilinear interpolation. Finally, the refined Lee filter [30] was applied to remove the speckle noise in SAR data.

C. DEM Data

The shoreline refers to the boundary area between a body of water, such as an ocean or sea, and adjacent land. According to the above definition, the dynamic changes of shoreline boundaries are easily affected by sediment movement and tidal fluctuations in the coastal zone [31]. In addition, there are some errors in SAR shoreline detection due to SAR geometric distortion, which has been shown in our previous study [29].

Fig. 2 shows that the shoreline changes with tide levels on sandy beaches and intertidal zones. It can be observed that the shoreline of the intertidal zone is significantly different at high tide and low tide, indicated in the blue circle area in Fig. 2(a). However, due to the limitations of beach width (approximately less than 80 m in Taiwan) and the resolution of Sentinel-1, the difference in shoreline changes in the beach area is relatively small, as shown in Fig. 2(b). Tidal level is indeed an important factor in mapping the extent or area of beaches and intertidal zones. In the study, a shoreline detection method was proposed to obtain the boundary between sea and land based on SAR images. Therefore, the corresponding shoreline can be detected at high or low tide, as displayed in Fig. 2. In subsequent experiments, the reference shoreline provided by CPAMI was used to verify the accuracy of the detected shoreline. Considering that the reference shoreline was delineated based on the high tide level, Sentinel-1 test images corresponding to high tide levels in the selected experimental regions were collected based on tidal information from the Taiwan Central Weather Bureau.

Next, the inherent error of geometric distortion in SAR data caused by radar side-looking shown [32], shown in Fig. 3, will affect the shoreline detection performance. Due to the

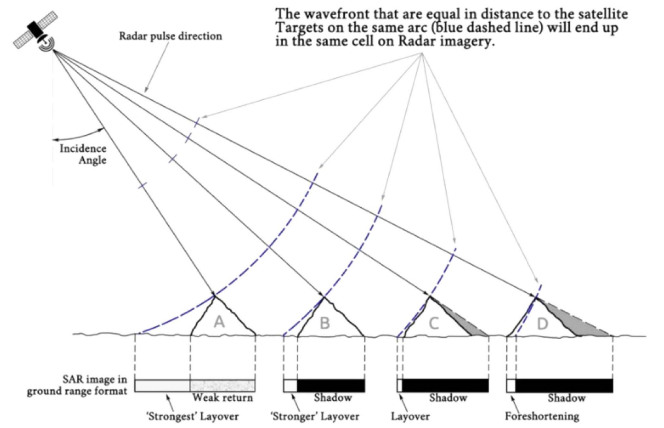


Fig. 3. Inherent errors in SAR data due to geometric distortion [32].

continuous collision and upward movement of the plates near Taiwan, the topography along the eastern coast of Taiwan is complex and rugged. Therefore, some areas with large slope fluctuations are affected by the geometric distortion due to the side-looking of Sentinel-1, especially in eastern fault coast of Taiwan.

As shown in the circled area in Fig. 4(a) and (b), due to the shadow effect of SAR, the radar backscatter value of these undulating areas is close to that of the water surface, which will affect the shoreline detection performance. DEM provides terrain elevation data and has become a useful technology in the fields of geography and engineering such as terrain analysis, simulation, and display. Since DEM elevation information truly reflects the topography of the SAR shadow area, it helps to better distinguish land and water topography, as shown in Fig. 4(c). This data can help the detection model reduce misclassifications caused by radar shadowing effects. Therefore, this study utilized the elevation information provided by the shuttle radar topography mission (SRTM) dataset [33] to mitigate land-sea segmentation errors in SAR geometrically distorted regions. The product Global 3 arc second SRTM DEM was applied in the research, which provides elevation data of the earth from 54°S to 60°N with about 90 m resolution. Although the resolution of this DEM is too coarse to compete with the Sentinel-1 SAR data for delineating shorelines in detail, the elevation information provided by the DEM helps reduce shorelines detection errors in SAR shadowed areas. Moreover, the DEM data at the boundary of land and water is not a specific value (0 m), making it challenging to define the exact location of the shoreline from DEM data. Since elevation information can alleviate the radar shadow effect, and SAR data can describe the details of the shoreline, the combination of DEM and SAR data can help improve the accuracy of shoreline detection. In addition, according to the backscattering characteristics of SAR images, the sigma-naught of Sentinel-1 VH polarization is more suitable for shoreline detection than VV polarization [34]. Based on the above considerations, this study combines Sentinel-1 VH polarization with DEM data to form the stacked input of the modified U-Net model, as shown in Fig. 4(d). For visualization purposes, this stacked data is shown in the pseudo color, where VH is red/green, and DEM is blue.

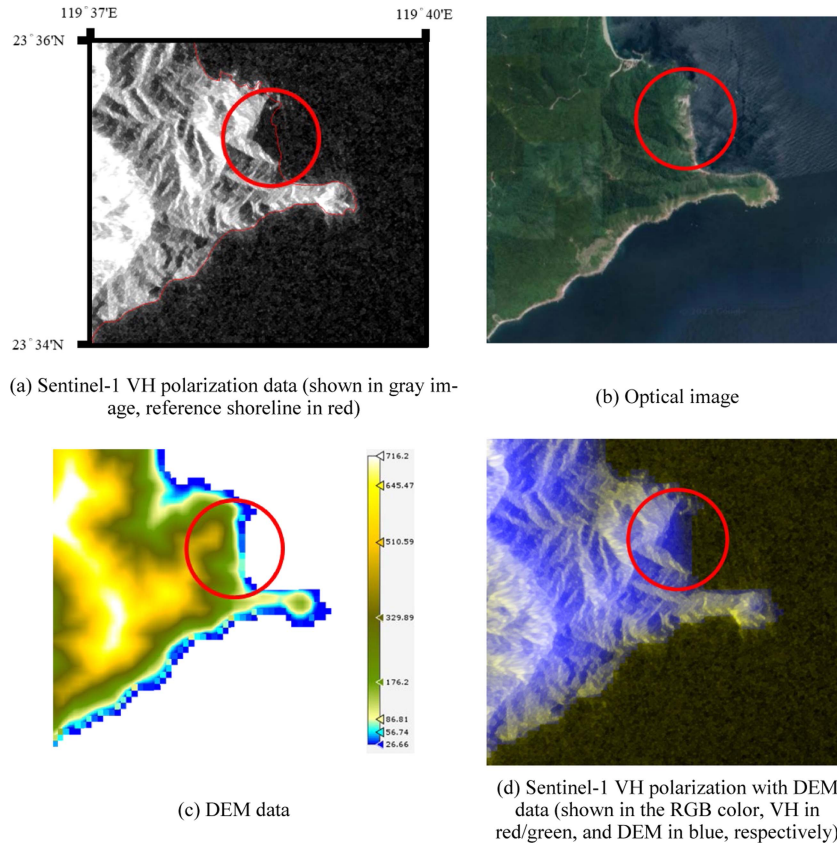


Fig. 4. Eastern coast of Taiwan affected by the geometric distortion. The sampling date of the image is September 17, 2016.

III. PROPOSED METHOD

To achieve shoreline detection, the land–sea segmentation was first performed in the study by using a semantic segmentation classifier that considers both pixel values and spatial context. U-Net is one of the widely used semantic segmentation models and has achieved superior segmentation performance in several studies [21], [22], [23], [25], [26]. In addition, the U-Net model based on CNN architecture can achieve fast and accurate image segmentation with fewer training images. In order to reduce the model parameters and computational burden of U-Net without affecting segmentation performance, this study modified the U-Net structure originally developed by Ronneberger et al. [20] to improve feature extraction of shorelines. Furthermore, a performance metric was proposed to evaluate the distance deviation of the detected shoreline from the reference data.

A. Modified U-Net

The modified U-Net model consisted of an encoder-CBAM-decoder architecture, where the encoder module was based on the MobileNetV3, as shown in Fig. 5.

The encoder (contraction path) captures contextual information and the symmetric decoder (expansion path) achieves precise positioning. MobileNetV3 is a state-of-the-art deep neural network architecture designed for efficient and accurate image classification tasks on resource-constrained devices, especially mobile and edge devices. It was developed to strike a balance

between model size, computational efficiency, and performance. In particular, MobileNetV3 achieved the highest top-1 accuracy among the different model considered by Howard et al., [27]. Therefore, the lightweight MobileNetV3 model was applied as the backbone architecture for this shoreline segmentation task.

MobileNetV3 introduced a novel inverted residual structure with linear bottlenecks, leveraging a lightweight depthwise separable convolution to reduce parameters and computational costs, as shown in Fig. 6. The integration of squeeze-and-excitation blocks was also a significant enhancement, selectively emphasizing informative channels to improve accuracy without adding substantial computational overhead. A standout feature was the dynamic inverted residuals, which can adapt to diverse input resolutions and computational budgets. This dynamic approach enhanced the model's flexibility for a variety application with different resource constraints. Moreover, the adoption of the Hard Swish activation function refined expressiveness while maintaining computational efficiency, striking a crucial balance for capturing complex data patterns without compromising performance.

In recent years, attention mechanisms have been widely used in extracting intricate image details and mitigating the impact of background noise on target features. The channel attention module focuses on determining the importance of different features within the image, while the spatial attention module prioritizes critical regions within those features. Within the channel attention module, the input feature maps undergo a pooling operation

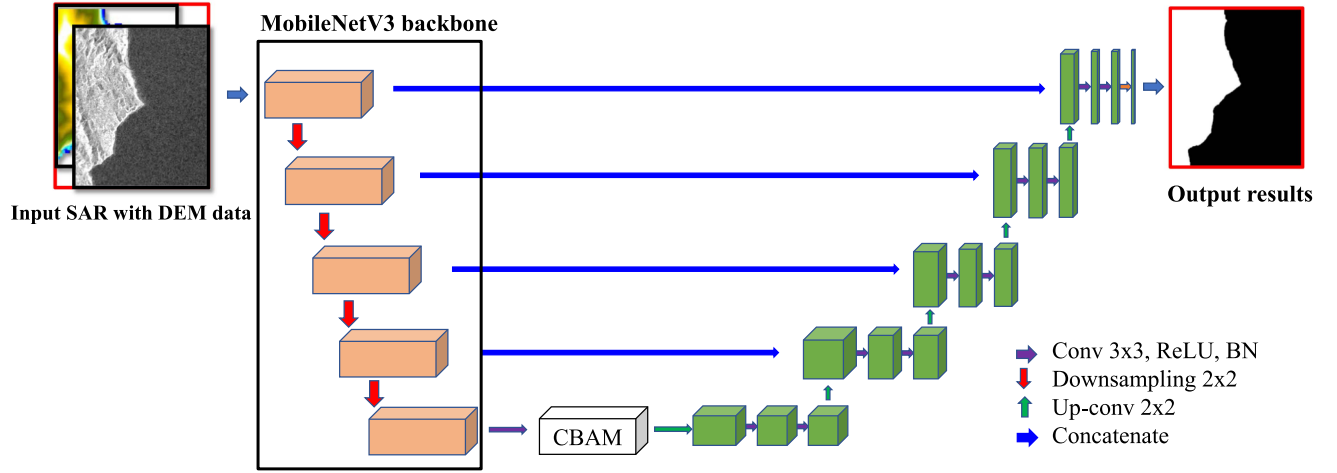


Fig. 5. Proposed modified U-Net architecture.

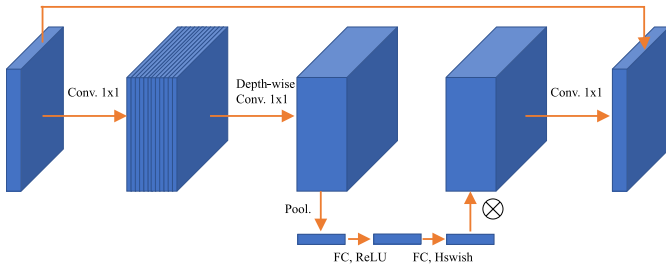


Fig. 6. MobileNetV3 block.

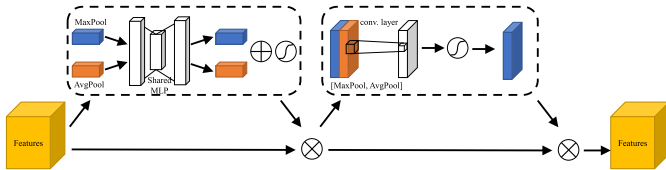


Fig. 7. CBAM attention mechanism.

to derive channel weights, which are subsequently applied to the spatial attention module. The spatial attention module computes the maximum and average values for each channel at every feature point. The obtained weights are then multiplied with the original input feature map and convolved, producing deep features enriched with multiscale contextual information. In this study, the CBAM attention mechanism consisted of two above modules was applied to the U-Net network, as shown in Fig. 7. In addition, a key advantage of CBAM is its lightweight nature, allowing integration into any neural network structure. Consequently, the CBAM module was incorporated at the end of the encoder, enhancing the feature extraction learning process.

The decoder part consisted of a 2×2 transposed convolution unit, which was concatenated with the previous encoder output, and then fed the result into two convolution blocks consisting of a 3×3 convolutional layer followed by an activation ReLU and a BN layer. The output of the decoder was then pooled through

a 1×1 convolution with the Sigmoid activation function to obtain the class prediction probability for each pixel. In order to extract the meaningful image information in dense feature vectors, the encoder gradually compresses the tensor, while the decoder gradually enlarges the tensor back to its original size, mapping the meaningful features to their respective locations.

Through subsequent experimental verification, the modified U-Net improves the performance of shoreline detection with the enhancement of feature extraction abilities and training stability.

B. Input and Output of Modified U-Net

The input of the modified U-Net model consists of VH polarization data and DEM data. The output result has the same size as the input image with two channels of classification probabilities for land and sea. However, the input image size is limited by GPU RAM and batch size. Therefore, the SAR image was divided into several subimages for the training of U-Net. The subimages were cropped with pixel overlap to avoid some performance degradation in segmentation. In the following experiments, the size of subimages and the number of overlapping pixels were chosen to be 256×256 and 50, respectively. After the segmentation of U-Net, it is necessary to perform edge detection and postprocessing for shoreline detection. In this study, the edge between the land and sea was extracted using Sobel [35] edge detection method. Afterward, the detected shoreline in the subimages were reoverlapped and merged back to the original image size. Due to some differences in the background and texture of each subimage, the shoreline detection results are not fully connected or consistent in the overlapping images. The discontinuity of the merged shoreline was postprocessed by the morphological image processing proposed in our previous study [29]. First, the closing and hole filling operations were used to connect the gaps between the detected shorelines in subimages. The thickened boundary was then iteratively removed by the morphological thinning operation while maintaining shoreline connectively. Finally, the branches generated by the thinning

operation were removed by morphological spurring operation and the shoreline detection results were obtained.

C. Performance Evaluation

In order to evaluate the performance of edge detection, it is necessary to quantitatively measure the edge different between the reference maps and the detection results through performance evaluation. Performance metrics such as precision, recall, or F1-score [36] are often used to measure the accuracy of object detection. The previous study [29] used the edge F1-measure to evaluate the shoreline detection accuracy. The detected edge point is considered to be correct if the distance between the detected edge point and the nearest reference edge point is less than N , where N represents the allowable distance difference. However, these metrics have the disadvantage in directly measuring the accuracy of shoreline position. In the study, a new performance metric dedicated to shoreline detection was proposed based on the statistics of the distance difference between detection results and reference edges. The proposed performance metrics can more intuitively evaluate the effectiveness of shoreline detection. The performance of shoreline detection can be evaluated by calculating the distance between the shoreline detection results from U-Net and manually delineated reference data, which is defined as follows:

$$d(i) = |P_{\text{shoreline}}(i) - R_{\text{shoreline}}(i)| \quad (1)$$

where $P_{\text{shoreline}}$ and $R_{\text{shoreline}}$ denote the prediction results of U-Net and the reference shoreline, respectively, $d(i)$ represents the distance difference between the i th edge point in the prediction result, $P_{\text{shoreline}}(i)$, and the corresponding point in the reference shoreline, $R_{\text{shoreline}}(i)$. Therefore, the mean and root mean square error (RMSE) can be used as the performance metrics to evaluate the shoreline detection

$$\text{Mean}_d = \frac{1}{N_p} \sum_{i=1}^{N_p} d(i) \quad (2)$$

$$\text{RMSE}_d = \sqrt{\frac{1}{N_p} \sum_{i=1}^{N_p} d^2(i)} \quad (3)$$

where N_p represents the total pixel number of the predicted shoreline.

However, it is difficult to search for the corresponding points between detection results and reference shorelines. Since the directions of the detected shorelines and reference shorelines were not consistent, the study [25], [37] first created reference baselines for fixed-distance-spaced (e.g., 200 m and 1 km in [25] and [37], respectively) vertical transects. Then, generated transect lines perpendicular to the baselines, which intersected the detected and reference shorelines. Finally, the shoreline performance was evaluated based on the distance between the intersection points in detected and reference shorelines. Instead of calculating the distance $d(i)$ directly, the probability function of the distance is measured. In the study, the number of detected edge points falling within t pixels of the reference shoreline is measured by morphological processing of image dilate by disk structuring element. As shown in Fig. 8(b), the reference

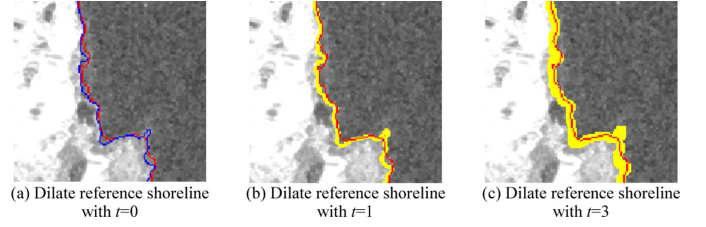


Fig. 8. Detected edge points within t pixels of reference shoreline. Detected result, reference shoreline and dilate reference with t -pixel are in red, blue and yellow, respectively.

shoreline was dilated by the dilating operation of morphological processing with 1-pixel disk structure element. Therefore, the number of edge points falling within the range of dilated reference shoreline in the detection results can be calculated, that is, the number of detected shorelines that are less than 1 pixel away from the reference shoreline. Similarly, for the reference shoreline dilated with t -pixel structure element, the number of edge points in the detection result that are less than t pixels away from the reference shoreline can be calculated, for example, $t = 3$ as shown in Fig. 8(c). As the pixel size of the structure element increases, the dilation process of the reference shoreline is continuous until all edge points in the detected shoreline are within the dilated reference shoreline. In this way, the probability function of t -pixel distance difference between the detected and reference shorelines can be obtained, which is defined as follows:

$$\text{Int}(t) = \text{No. of } (P_{\text{shoreline}} \cap R_{\text{shoreline}} \text{ (with } t \text{ pixel dilation)}) \quad (4)$$

where “ \cap ” denotes the intersection and $\text{Int}(t)$ represents the numbers of the detected edge points falling within t pixels of the reference shoreline. From (4), the probability function of t -pixel distance between the detected and reference shorelines can be obtained by calculating the difference between $\text{Int}(t)$ and $\text{Int}(t-1)$, and dividing it by the length of detected shoreline

$$\text{Pr}(t) = \frac{\text{Int}(t) - \text{Int}(t-1)}{N_p} \text{ for } t = 1, \dots, M \quad (5)$$

with $\text{Pr}(0) = \text{Int}(0)/N_p$. In (5), M is the maximum distance difference. Therefore, the shoreline detection performance can be statistically analyzed according to the probability function of distance. The mean and RMSE shown in (2) and (3) can be recalculated as follows:

$$\text{Mean}_d = \sum_{t=0}^M t \text{Pr}(t) \quad (6)$$

$$\text{RMSE}_d = \sqrt{\sum_{t=0}^M t^2 \text{Pr}(t)}. \quad (7)$$

In addition, the statistical model of the cumulative distribution function (CDF) of distance difference, obtained from (5), is used for the evaluation of shoreline detection in subsequent

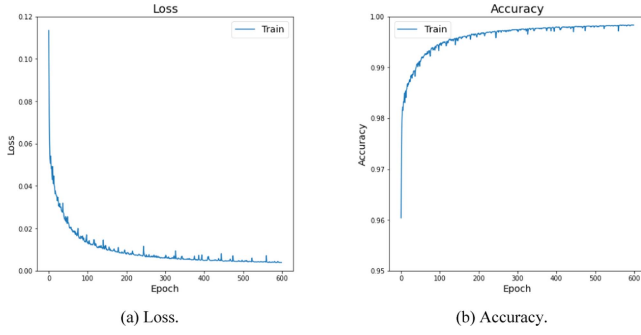


Fig. 9. Training process of the proposed U-Net network using SLS1 DEM dataset.

experiments

$$\text{CDF}(t) = \frac{\text{Int}(t)}{N_P}. \quad (8)$$

IV. RESULTS

A. Experimental Settings

All experiments were performed on a PC equipped with 10 GB memory of NVIDIA GeForce RTX3080, 16 GB memory of Intel Core i7-8700k, and using cuDNN 8.0.4 with CUDA 11.0. The operating system was Windows 10 64-bit. The study has collected the Sentinel-1 images along the coastal areas of Taiwan and the reference data provided by CPAMI. The images were divided into several subimages of the size 256×256 with 50 pixels overlap. In addition, there are two self-built shoreline datasets, including ShoreLine detection using Sentinel-1 (SLS1) dataset composed of Sentinel-1 VH polarization images extended by previous studies [29], and new ShoreLine detection using Sentinel-1 and DEM (SLS1 DEM) dataset composed of Sentinel-1 VH polarization images and DEM data. SLS1 and SLS1 DEM dataset contained a total of 4061 and 3822 images, respectively, collected from 2016 to 2019. The corresponding annotation sets were then generated by labeling the images using morphological processing and Otsu's thresholding method. The performance metrics mean, RMSE, and F1-measure [29] were utilized to evaluate the shoreline detection performance of the U-Net models. In addition, F1-measure was calculated with 5-pixel distance difference between detection results and reference data in the following experiments.

In this study, the shoreline datasets were divided into 90% training images and 10% testing images. During training, the batch size and the number of epochs were set to 16 and 600, respectively. The Adam optimizer [38] and binary cross-entropy loss function were selected to train the U-Net models. The learning rate was set to 0.0001 and an early stopping was set by monitoring the value of loss function. The training process of the modified U-Net model using SLS1 DEM dataset was shown in Fig. 9, achieving an accuracy of 0.9981 and a loss of 0.0021. The training process of the modified U-Net using SLS1 dataset was similar to that in Fig. 9, with an accuracy of 0.9905 and a loss of 0.0035.

TABLE II
DETECTION ACCURACY OF U-NET MODELS ON SLS1 AND SLS1 DEM DATASETS

Input data		Original U-Net	U-Net with BN	Modified U-Net
SLS1	Mean	0.3272	0.3201	0.2514
	RMSE	0.7034	0.6922	0.6071
	F1-measure	0.9213	0.9462	0.9862
SLS1 DEM	Mean	0.2516	0.2246	0.1984
	RMSE	0.5026	0.4194	0.3845
	F1-measure	0.9381	0.9897	0.9902

In addition, the study further compared the modified U-Net model with other shoreline detection algorithms, including improved Fuzzy C-means (IFCM) [37] and statistical model of sea (SMS) [39]. The IFCM [37] combined Fuzzy C-means with Wavelet decomposition algorithm to improve the shoreline detection performance. The SMS [39] determined the sea-land separation threshold based on an adaptively established statistical model of the sea area, and removed misclassified land areas by comparing the variance difference between the statistical models of land and sea.

B. Overall Accuracy

In this experiment, the study compared the shoreline detection performance of the modified U-Net approach on two constructed datasets. Using the testing data of these two datasets, the shoreline detection accuracy of different U-Net models was evaluated, as listed in Table II, including original U-Net, U-Net with BN [29] and the proposed modified U-Net. Compared with the original U-Net, the proposed modified U-Net used MobileNetv3 as the backbone of the encoder and added CBAM attention mechanism to improve the detection performance.

First, the study compared the detection performance of three different U-Net models using SLS1 dataset. From the results in Table II, it can be observed that the proposed modified U-Net performed the best, with a mean of 0.2514 and RMSE of 0.6071 pixels, lower than those of original U-Net and U-Net with BN, as shown in Table II. Then, the U-Net with BN performed slightly better than the original U-Net model. Moreover, the F1-measure of the proposed modified U-Net achieved about 0.9862, which was 0.065 and 0.04 higher than the original U-Net and U-Net with BN, respectively. The results showed that the proposed modified U-Net achieved more accurate shoreline detection than the other two models when using only SAR data.

Next, the shoreline detection performance of U-Net models was examined on SLS1 DEM dataset consisting of Sentinel-1 SAR and DEM data. The detection result of the original U-Net was still the worst one among the three U-Net models. The proposed modified U-Net performed best when using both SAR and DEM data. The average distance difference between the detection results of the proposed modified U-Net and the annotated shoreline was 0.1984 pixels, which was lower than that of U-Net with BN model by 0.0262 pixels. The experimental results still validated that the proposed modified U-Net achieved highest shoreline detection accuracy than the original U-Net. For all three U-Net models, the average distance difference of the model trained by SLS1 DEM dataset was smaller than that of the corresponding model trained by SLS1 dataset. The results

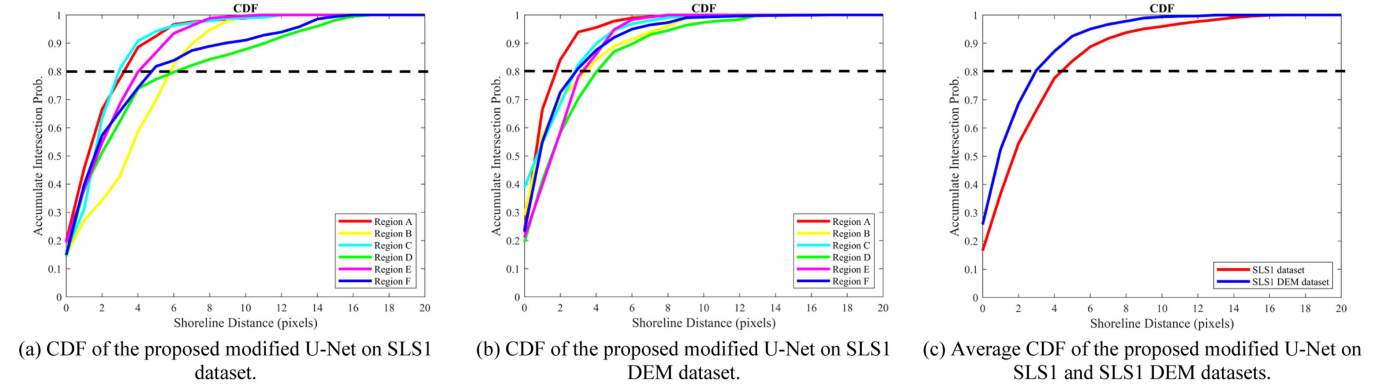


Fig. 10. CDF curves of shoreline detection by the proposed modified U-Net on SLS1 and SLS1 DEM datasets.

TABLE III
INFORMATION OF THE SIX SELECTED REGIONS

Region	Geographic location	Source	Acquisition dates	Tidal level(cm)
A	120°52'E to 120°55'E, 22°00'N to 22°03'N	S1A(Ascending)	November 16, 2016 10:00	90
		S1A(Descending)	October 20, 2017 21:52	88
		S1A(Descending)	July 11, 2018 21:52	98
		S1A(Descending)	September 28, 2019 21:52	115
B	120°09'E to 120°12'E, 22°52'N to 22°54'N	S1A(Ascending)	January 9, 2016 10:00	68
		S1A(Descending)	June 22, 2017 21:52	82
		S1A(Descending)	July 11, 2018 21:52	101
		S1A(Descending)	July 30, 2019 21:52	103
C	120°39'E to 120°44'E, 24°29'N to 24°35'N	S1A(Ascending)	October 23, 2016 10:00	184
		S1A(Ascending)	April 21, 2017 10:01	173
		S1A(Ascending)	July 21, 2018 10:01	182
		S1A(Ascending)	August 9, 2019 10:01	183
D	121°39'E to 121°44'E, 24°10'N to 24°14'N	S1A(Ascending)	September 17, 2016 10:00	110
		S1A(Ascending)	October 6, 2017 10:01	93
		S1A(Ascending)	April 16, 2018 10:00	60
		S1A(Ascending)	November 25, 2019 10:01	61
E	121°52'E to 121°57'E, 24°54'N to 24°57'N	S1A(Ascending)	November 16, 2016 10:00	87
		S1A(Descending)	June 22, 2017 21:52	90
		S1A(Ascending)	September 7, 2018 10:01	71
		S1A(Ascending)	November 25, 2019 10:01	92
F	121°47'E to 122°01'E, 25°00'N to 25°08'N	S1A(Ascending)	October 23, 2016 10:00	68
		S1A(Ascending)	August 31, 2017 10:00	53
		S1A(Ascending)	July 21, 2018 10:01	55
		S1A(Ascending)	August 9, 2019 10:01	72

in Table II validated the performance improvement of shoreline detection by using both Sentinel-1 SAR and DEM data.

C. Shoreline Detection Performance of Different Coastal Landforms

This experiment evaluated the shoreline detection performance of the proposed modified U-Net for different types of coastal landforms. In experiments, six test regions were selected, including coral reef coast, headland bay coast, sandy coast, and fault coast, as shown in Fig. 1. In addition, the shoreline detection results were compared with the reference data provided by CPAMI. Considering that the reference coastline provided by CPAMI was delineated based on high tide level, the Sentinel-1 image with the highest tide level among all Sentinel-1 SAR images collected within a year was selected for the experiment. Table III showed the information of the selected images for each test region from 2016–2019.

Evaluation metrics included mean, RMSE, and F1-measure, which were the average of the four-year detection results, as shown in Table IV and Fig. 10. However, the detection results

of SMS and IFCM methods on SLS1 DEM dataset were relatively fragmented, resulting in low efficiency of the shoreline detection. Therefore, only the detection results of these two methods on SLS1 dataset were compared in the experiments. For an overall evaluation of all coastal landforms, the last column of Table IV presented the average values of the corresponding performance metrics for the six selected regions.

First, compare the detection results of the three U-Net models on SLS1 dataset from Table IV. It can be observed that the detection performance of the proposed modified U-Net was consistently better than the other two U-Net models in all selected regions, with an average mean value of 4.01 pixels, about 0.79 and 0.56 pixels smaller than the original U-Net and U-Net with BN, respectively. The detection results of IFCM on SLS1 dataset were close to original U-Net in Regions B, and C, but worse than original U-Net in Regions A, D, E, and F. The average Mean of IFCM was 5.55 pixels, about 0.75 pixels larger than original U-Net. In general, SMS performed worse than the original U-Net in selected regions.

Next, the detection performance of the three U-Net models on SLS1 DEM dataset was examined. From Table IV, the original U-Net performed the worst, with an average mean of 2.70 pixels, which was 0.44 and 0.68 pixels larger than the U-Net with BN and the proposed modified U-Net, respectively. For all selected regions, the detection results of the proposed modified U-Net were still better than the other two U-Net models. Furthermore, the proposed modified U-Net layers achieved mean F1-measures of 0.91 for the selected regions, which meant that more than 91% of shoreline detected within 5-pixel distance difference.

Then, the shoreline detection performance of the U-Net models on the two datasets was evaluated for different coastal landforms. For comparison, the CDF curves of the detection results of the modified U-Net model in selected regions were shown in Fig. 10. The performance was compared based on the minimum distance difference (t pixels) between the detection result and the reference map for each region when the CDF value reached 0.8. That is, more than 80% of the shoreline can be detected within t -pixel distance difference from the reference data. The results in Fig. 10(a) showed the CDF curve of the proposed modified U-Net on SLS1 dataset for each region. The detection performance was better in Regions A, C, and E, slightly worse in

TABLE IV
DETECTION PERFORMANCE EVALUATION OF SIX SELECTED REGIONS BY COMPARING THE MODIFIED U-NET MODELS WITH OTHER SHORELINE DETECTION METHODS

Input data	Method		Region						Average
			A	B	C	D	E	F	
SLS1	SMS	Mean	4.22	5.96	3.45	8.16	5.81	5.16	5.46
		RMSE	3.74	4.61	4.48	7.71	4.72	4.71	5.00
		F1-measure	0.72	0.48	0.63	0.48	0.67	0.62	0.60
	IFCM	Mean	4.80	5.43	3.21	7.77	6.65	5.46	5.55
		RMSE	3.95	4.87	2.81	7.64	4.54	4.64	4.74
		F1-measure	0.70	0.51	0.65	0.50	0.61	0.71	0.61
	Original U-Net	Mean	3.55	5.40	2.96	7.15	4.98	4.74	4.80
		RMSE	3.23	3.17	2.51	8.49	3.15	5.79	4.39
		F1-measure	0.84	0.51	0.87	0.67	0.71	0.73	0.72
	U-Net with BN	Mean	3.28	5.05	2.94	6.89	4.77	4.51	4.57
		RMSE	2.82	3.09	2.70	8.36	3.13	5.72	4.30
		F1-measure	0.85	0.52	0.88	0.70	0.75	0.73	0.74
	Modified U-Net	Mean	2.87	4.59	2.49	5.88	4.24	3.99	4.01
		RMSE	2.67	2.88	2.03	7.24	2.92	5.26	3.88
		F1-measure	0.88	0.60	0.91	0.77	0.85	0.79	0.80
SLS1 DEM	Original U-Net	Mean	1.66	3.88	2.40	3.34	2.64	2.26	2.70
		RMSE	1.42	2.83	1.73	2.67	2.09	2.70	2.24
		F1-measure	0.93	0.70	0.91	0.85	0.86	0.87	0.85
	U-Net with BN	Mean	1.38	2.46	2.42	3.37	2.29	1.61	2.26
		RMSE	1.06	2.21	1.96	2.79	1.78	2.10	1.98
		F1-measure	0.96	0.85	0.90	0.83	0.89	0.93	0.89
	Modified U-Net	Mean	1.26	2.27	2.08	2.83	2.23	1.48	2.02
		RMSE	1.00	1.90	1.84	3.03	1.69	1.82	1.88
		F1-measure	0.96	0.86	0.92	0.88	0.89	0.94	0.91

Region F, and the worst in Regions B and D. It can be observed that the minimum distance differences for Regions A to F were 3, 6, 3, 6, 4, and 5 pixels, respectively. From Fig. 10(b), the results of the proposed modified U-Net on SLS1 DEM dataset showed that for all the selected regions, the minimum distance difference required to achieve a CDF value of 0.8 was smaller than the corresponding value in Fig. 10(a). In addition, from the detection results of the two datasets, it can be found that the average shoreline distance difference of the proposed modified U-Net on SLS1 DEM dataset was about half of that of the detection results on SLS1 dataset. Overall, the modified U-Net using SAR and DEM inputs can effectively improve the shoreline detection performance.

Compared with the F1-measure, the proposed CDF can evaluate the overall result of shoreline detection. According to the F1-measure of the proposed modified U-Net on SLS1 dataset, Region B performed the worst. Moreover, it can be seen from the CDF curves in Fig. 10(a) that the maximum distance difference between the detection result of Region B and the reference shorelines was 10 pixels, which was much smaller than the 16 pixels of Region D. The distance difference between some detected shorelines and the reference shorelines was relatively large, resulting in the Mean value of 5.88 pixels in Region D being greater than that of 4.59 pixels in Region B, as shown in Table IV. In addition, the average CDF of all regions detected by the proposed modified U-Net was shown in Fig. 10(c). It can be observed that the shoreline detection performance using SLS1 DEM dataset was better than SLS1 dataset. When the CDF value reached 0.8, the corresponding distance differences of SLS1 DEM and SLS1 dataset were about 3 and 5 pixels, respectively. Compared with the results in Table III, the poorer detection results in Table IV were due to the complex coastal landforms or man-made structures in the six selected regions.

Furthermore, the proposed CDF can present the distance difference distribution of detected shoreline, and performance metrics Mean and RMSE can show the statistical analysis of detection results. The experiments validated the performance improvement for shoreline detection using the combined SAR and DEM data.

V. DISCUSSION

This study utilized the elevation information provided by DEM to mitigate the shoreline detection error caused by radar shadowing effect. In the Copernicus DEM, the elevation 0 m refers to the mean sea level of the DEM vertical reference datum (i.e., Earth Gravity Model 2008—EGM 2008). Since the DEM data do not always equal 0 m at the shoreline, the boundary between land and water, it is difficult to define the exact location of the shoreline directly from the DEM data. From the experimental results in previous section, the elevation information can improve shoreline detection accuracy, although the resolution of the DEM is poor compared to Sentinel-1 data.

In the study, the reference data provided by CPAMI of Taiwan, were applied to verify the effectiveness of the proposed method. CPAMI spends a lot of time, cost, and manpower on shoreline mapping every year. In addition, the study area has a vast coastline and complex coastal topography, which poses challenges to rapid detection of shoreline changes. SAR data have been proved to be an effective tool for shoreline detection because of its wide coverage, strong penetration, and all day/weather imaging observations. Moreover, climate change and global warming lead to changes in sea level and shoreline, which pose a huge threat to island of Taiwan. Through long-term and multitemporal SAR data acquisition, the proposed method provides feasibility for shoreline detection and timely monitoring of shoreline

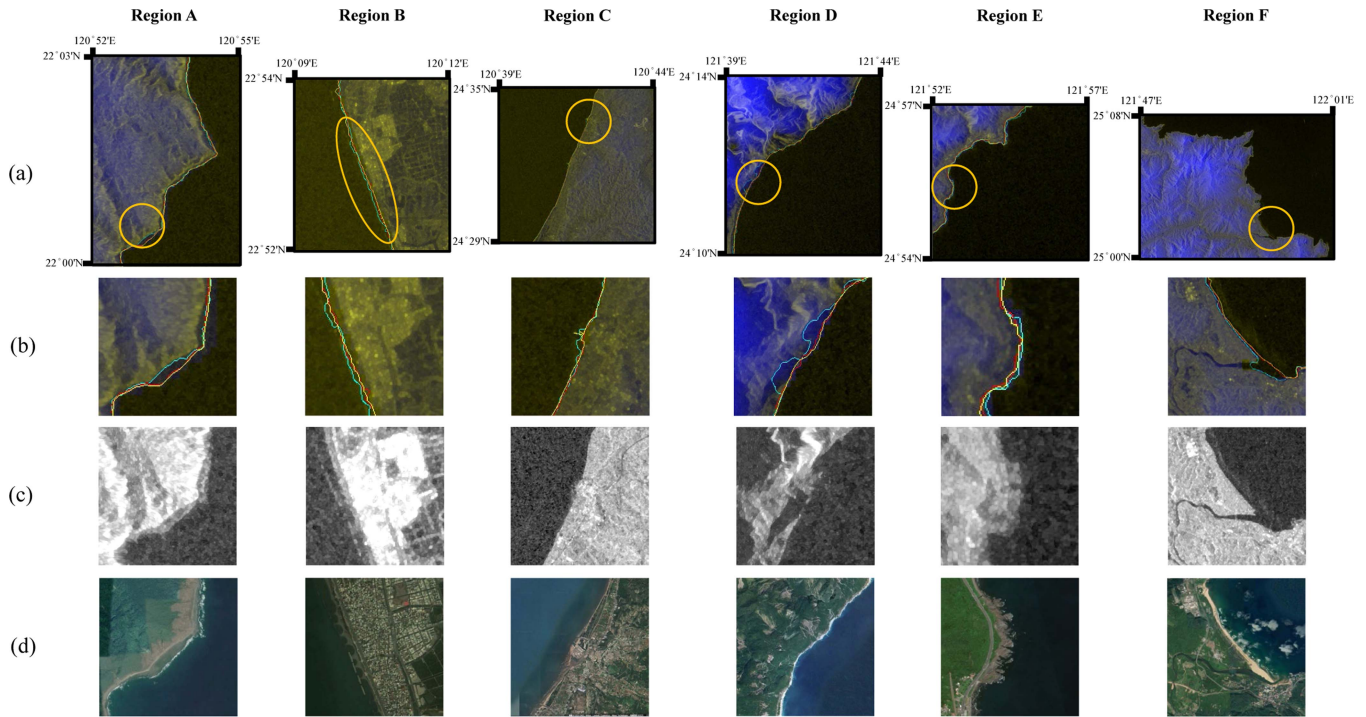


Fig. 11. Shoreline detection results for different regions of the study area. The cyan and red borders represent the detection results of the SLS1 and SLS1 DEM datasets, respectively. The yellow border represents the reference data. (a) Shoreline detection results of six selected regions (Regions A–F from top to bottom). (b) Orange circled area of the image in (a). (c) Corresponding VH polarization data of the area circled in orange. (d) Corresponding optical images of the area circled in orange. The sampling date of Region A is September 28, 2019, Region B is July 30, 2019, Region C is October 23, 2016, Region D is September 17, 2016, Region E is 2019/11/25, Region F is August 9, 2019, with detailed information shown in Table III.

changes. Therefore, this study improved the shoreline detection accuracy by combining SAR and DEM data, not only using DEM information to alleviate the radar shadow effect, but also using SAR data to describe the details of the shorelines.

A. Effect of Coastal Topography on Shoreline Detection Performance

Observing the experimental results in Tables III and IV, it can be clearly seen that the shoreline detection results of the six selected regions shown in Table IV were worse than those in Table III. Table III showed the average detection results of all coastal areas randomly selected from the constructed dataset. To explore the main reasons for the poor detection results in the six selected regions, the detected shorelines of these regions were examined and the impact of complex coastal topography on detection performance was discussed in the following. Fig. 11 depicted the shorelines detected by the modified U-Net model for each region, where the detection results using SLS1 and SLS1 DEM datasets were shown in cyan and red, respectively, and the reference shorelines were shown in yellow. The detected shorelines, the area with a large deviation of the detected shoreline, the SAR image and the optical image were displayed in Fig. 11(a)–(d), respectively.

There are some coral reefs along the coast of Region A. As shown in the first row of Fig. 11(a), the distribution of coral reefs is relatively scattered, resulting in weak SAR backscatter reflection coefficient and more tortuous shoreline detection results.

Parts of the shoreline cannot be accurately detected using SLS1 dataset, which led to a large discrepancy between the detection results and the reference data, especially the area circled in orange. These misclassifications can be observed in the first row of Fig. 11(b)–(d) by comparing the detection results using SLS1 dataset with the optical image. However, the shoreline depicted by the modified U-Net using SLS1 DEM dataset was close to the reference data, e.g., the shoreline can be detected more accurately in the orange circle area.

Region B is a sandy coast located in the southwestern part of Taiwan. There are many breakwaters and artificial beaches along the coast of this region, as shown in the second row of Fig. 11(d). The modified U-Net model detected the man-made developments as shorelines due to their large backscatter values in the SAR image. However, these man-made developments were not considered as shorelines in the reference data according to human subjective perception. Therefore, due to the influence of human cognition, there was a large difference between the shorelines detected using SLS1 dataset and the reference data. With the assistance of DEM data, the shorelines detected by modified U-Net model using SLS1 DEM dataset appeared smoother and closer to the reference data. Region C, located in the northwest of Taiwan, is also a sandy coast, but the shoreline changes less than that of Region B. The detection results using SLS1 and SLS1 DEM datasets were closely to the reference data, except for the embankment of the port. These man-made structures cannot be accurately detected due to the resolution of the SAR data.

TABLE V
DETECTION PERFORMANCE EVALUATION OF SIX SELECTED REGIONS IN 2020

Input data	Method		Region						Average
			A	B	C	D	E	F	
SLS1	Proposed U-Net	Mean	2.58	5.26	4.09	6.39	4.84	4.12	4.55
		RMSE	2.81	3.06	3.94	6.97	3.08	5.28	4.19
		F1-measure	0.89	0.58	0.80	0.75	0.79	0.77	0.76
SLS1 DEM	Proposed U-Net	Mean	1.09	1.51	3.09	2.97	2.49	2.08	2.21
		RMSE	0.87	1.54	2.81	2.91	1.81	2.35	2.05
		F1-measure	0.96	0.86	0.86	0.85	0.89	0.91	0.89

Region D is a fault coast in the east of Taiwan, and the terrain in this area is relatively undulating. Due to the serious influence of SAR geometric distortion, the shoreline detection performance in the region was worse than other regions. By comparing the SAR image with the optical image in the fourth row of Fig. 11(c) and (d), the radar shadow can be clearly found. Therefore, it can be observed that the shoreline detection results using SLS1 dataset in the orange circle were affected by the radar shadows, resulting in a large difference from the reference shoreline. However, the effect of terrain distortion can be mitigated by adding DEM data to the input of the modified U-Net. From Fig. 10 and Table IV, it can be seen that the modified U-Net model using SLS1 DEM dataset achieved a large improvement in shoreline detection in Region D compared to the U-Net model using SLS1 dataset.

There are some wave-cut platforms along the coast of Region E located in the northwest of Taiwan. The wave-cut platforms, like man-made developments in Region A, are not identifiable as shorelines in the reference data from a human perspective. As shown in the fifth row of Fig. 11(b), the shoreline detection results using SLS1 DEM dataset were closer to the reference data than those using SLS1 dataset. Region F is a headland bay in northern Taiwan, with some estuaries and harbors. The shoreline detection results using both datasets were close to the reference data, except for some harbors and estuaries within the orange circle in the sixth row of Fig. 11(a). The experiments validated that the modified U-Net model can effectively improve the shoreline detection performance on SAR images. However, inherent errors in SAR data due to geometric distortion and human development in coastal areas can affect shoreline detection performance. This study combined SAR and DEM data as the input of the modified U-Net model to alleviate the above problems, and greatly improved the performance of shoreline detection.

B. Generalization Ability of the Shoreline Detection Model

Furthermore, to examine the ability of the modified U-Net for shoreline detection on SAR images not included in the datasets, the proposed modified U-Net was applied to estimate the shorelines of Taiwan using SAR images acquired in 2020. The detection results of the six selected regions in Fig. 1 were summarized in Table V. It can be observed that the shoreline detection results of all six regions in Table V were very close to those in Table IV. The average mean of distance difference between the detected shoreline and reference data was 0.54 and 0.19 pixels higher than those in Table IV for the U-Net models trained with SLS1 and SLS1 DEM datasets, respectively. These

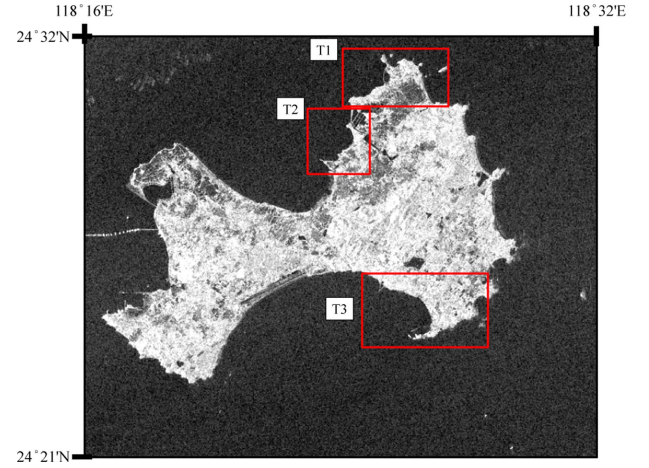


Fig. 12. VH polarization data of Kinmen island. The sampling date is July 27, 2020.

results verified the excellent performance of the modified U-Net in the shoreline prediction of the study area.

Then, the shoreline detection performance of the proposed modified U-Net was further evaluated using the Kinmen island, located 187 km west of the main island of Taiwan across the Taiwan Strait, which is not included in the built shoreline datasets. The Kinmen island is between 118°16'E to 118°30'E longitude and 24°21'N to 24°32'N latitude, with the image size of 2448 × 2013 pixels, as shown in Fig. 12. Three regions T1–T3 in Fig. 12 were selected to examine the predictive ability of the modified U-Net in shoreline detection. The shoreline detected by the proposed modified U-Net, SAR image and corresponding optical image of the selected regions in Fig. 12 were shown in Fig. 13. The detection results of the U-Net models trained with SLS1 and SLS1 DEM datasets were shown in cyan and red, respectively, while the reference shorelines were displayed in yellow.

Most of the detection shoreline was close to the reference shoreline except for the coastal areas circled in the selected regions. Since the SAR data was acquired at a relative high tide level, the reflection backscatter coefficient of the shoal coast circled in Region T1 is weak in SAR images, thus causing discrepancies between the detected shorelines and reference shorelines. For Region T1, the mean values of shoreline deviation detected by the modified U-Net on SLS1 and SLS1 DEM datasets were 3.89 and 1.76 pixels, respectively.

The coastal area circled in Region T2 is covered by the vegetation, resulting in significant backscattering in the SAR data. The proposed U-Net models using SLS1 dataset can accurately detect shorelines along vegetated coasts, which were not considered shorelines in the reference data. For Region T2, the mean values of shoreline deviation detected by the modified U-Net on SLS1 and SLS1 DEM datasets were 7.36 and 1.54 pixels, respectively. With the assistance of DEM information, the shoreline detected by the modified U-Net on SLS1 DEM dataset was close to the reference data in Regions T1 and T2.

As shown in the circled area of Region T3, the model trained by SLS1 cannot accurately detect narrow embankments.

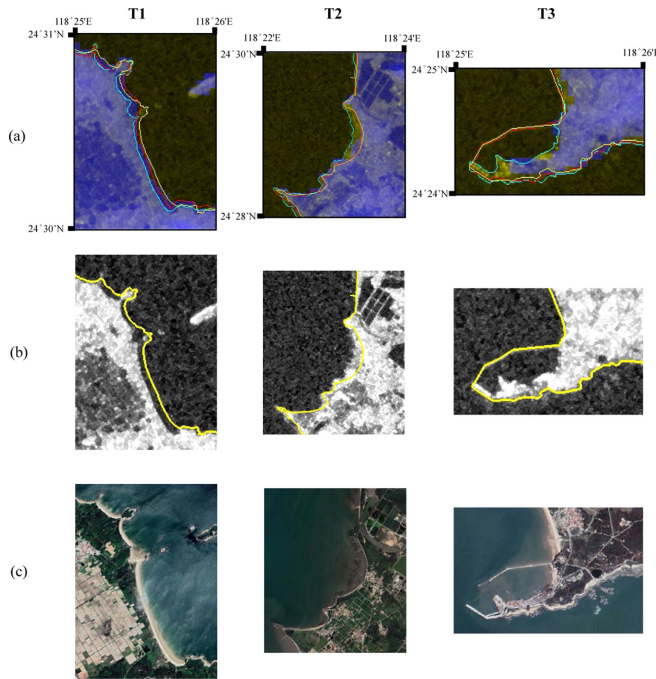


Fig. 13. Shoreline detection results of three selected regions in Fig. 12. The cyan and red borders represent the detection results of the SLS1 and SLS1 DEM datasets, respectively. The yellow border represents the reference data. (a) Shoreline detection results of three selected regions (Regions T1–T3 from left to right). (b) Corresponding VH polarization data and reference shoreline. (c) Corresponding optical images.

However, the model trained by SLS1 DEM can detect embankments through the information provided by DEM, and obtain shoreline results closer to the reference shoreline. For Region T3, the Mean values of shoreline deviation detected by the modified U-Net on SLS1 and SLS1 DEM datasets were 4.73 and 2.04 pixels, respectively.

For the modified U-Net model using SLS1 DEM dataset, the average mean of the three selected regions T1–T3 was 1.78 pixels, which was better than the detection results using SLS1 dataset with an average mean of 5.33 pixels. These results showed that the detected shorelines using the combination of SAR and DEM data were closer to the reference data than using SLS1 dataset. These experimental results validated the stable shoreline detection performance of the modified U-Net using SAR and DEM data in different test areas.

VI. CONCLUSION

This study proposed a modified U-Net model with inputs of SAR and DEM data to improve shoreline detection performance. In addition, the study provided a probabilistic model of the distance difference between the detected shoreline and the reference data. Based on the proposed CDF model, shoreline detection performance was evaluated using statistical analysis. Experiments were performed on two constructed datasets, one including Sentinel-1 SAR and the other consisting of Sentinel-1 SAR and DEM data. The detection accuracy of the modified U-Net was first investigated on the test data of the built datasets. Compared with the annotated shoreline, the modified U-Net

model achieved an average distance difference of 0.19 pixels, about 0.13 pixels lower than the original U-Net using Sentinel-1 SAR images. Then, the performance of the modified U-Net model was examined on six selected complex coastal landforms, including coral reefs, rocky, sandy, and headland bays. Due to the complex coastal landform in the selected regions, the shoreline detection performance of the original U-Net on SLS1 dataset was poor, with average distance differences of 4.80 pixels. However, the average distance difference between the shorelines detected by modified U-Net and the reference data was 2.02 pixels. Thus, the modified U-Net using SAR and DEM data can improve the shoreline detection performance, reducing the distance deviation from the CPAMI reference by more than 50% in the selected regions compared with the original U-Net using SAR. Experimental results demonstrated that the combination of SAR and DEM data can improve the shoreline detection performance for different coastal landforms, especially for the misclassified areas caused by radar shadows in SAR images. Finally, the shoreline detection capability of the modified U-Net model was verified by SAR images in different years and test areas, and the detection results validated the stable performance of the proposed method when extended to regions and acquisition times different from the dataset. In conclusion, the modified U-Net using SAR and DEM data can effectively improve the shoreline detection performance.

REFERENCES

- [1] W. Eric and A. Fie, "Protective functions of coastal forests and trees against natural hazards," in *Proc. Reg. Tech. Workshop*, Aug. 2006, pp. 157–159.
- [2] Y. Shih, "Coastal Management and implementation in Taiwan," *J. Coast. Zone Manage.*, vol. 19, no. 4, 2016, Art. no. 437.
- [3] J. S. Shen, J. S. Zhai, and H. T. Guo, "Study on coastline extraction technology," *Hydrography Surv. Charting*, vol. 2013, no. 20, pp. 74–77, 2009.
- [4] A. Buono, F. Nunziata, L. Mascolo, and M. Migliaccio, "A multipolarization analysis of coastline extraction using X-Band COSMO-SkyMed SAR data," *IEEE J. Sel. Topics Appl. Earth Obs. Remote Sens.*, vol. 7, no. 7, pp. 2811–2820, Jul. 2014.
- [5] M. Zhang, X. Z. Jiang, J. R. Zhang, and B. Tian, "Developments of coastline detection with remote sensing data," *Yellow River*, vol. 30, pp. 7–9, 2008.
- [6] T. Zhang, X. Yang, S. Hu, and F. Su, "Extraction of coastline in aquaculture coast from multispectral remote sensing images: Object-based region growing integration edge detection," *Remote Sens.*, vol. 5, no. 9, pp. 4470–4487, 2013.
- [7] R. Gens, "Remote sensing of coastlines: Detection, extraction and monitoring," *Int. J. Remote Sens.*, vol. 31, pp. 1819–1836, 2010.
- [8] J. E. Pardo-Pascual et al., "Assessing the accuracy of automatically extracted shorelines on microtidal beaches from Landsat 7, Landsat 8 and Sentinel-2 imagery," *Remote Sens.*, vol. 10, no. 2, 2018, Art. no. 326.
- [9] A. Al Fugura, L. Billa, and B. Paradhan, "Semi-automated procedures for shoreline extraction using single RADARSAT-1 SAR image," *Estuaries Coast. Shelf Sci.*, vol. 95, no. 4, pp. 395–400, 2011.
- [10] Z. Zhu, C. E. Woodcock, J. Rogan, and J. Kellndorfer, "Assessment of spectral, polarimetric, temporal, and spatial dimensions for urban and peri-urban land cover classification using Landsat and SAR data," *Remote Sens. Environ.*, vol. 117, pp. 72–82, 2012.
- [11] M. Modava, G. Akbarizadeh, and M. Soroosh, "Integration of spectral histogram and level set for coastline detection in SAR images," *IEEE Trans. Aerosp. Electron. Syst.*, vol. 55, no. 2, pp. 810–819, Apr. 2019.
- [12] C. Liu, Y. Y. Xiao, and J. Yang, "A coastline detection method in polarimetric SAR images mixing the region-based and edge-based active contour models," *IEEE Trans. Geosci. Remote Sens.*, vol. 55, no. 7, pp. 3735–3747, Jul. 2017.

- [13] U. Acar, B. Bayram, F. B. Sanli, S. Abdikan, F. Sunar, and H. I. Cetin, "An algorithm for coastline detection using SAR images," *ISPRS Arch.*, vol. 39, pp. 457–460, 2012.
- [14] L. Wu, Y. Tajima, Y. Yamanaka, T. Shimozono, and S. Sato, "Study on characteristics of SAR imagery around the coast for shoreline detection," *Coast. Eng. J.*, vol. 61, no. 2, pp. 152–170, 2019.
- [15] M. Mazzolini, M. Manzoni, A. V. Monti-Guarnieri, and M. Petrushevsky, "SAR-based coastline detection and monitoring," *ISPRS Arch.*, vol. 43, pp. 327–334, 2021.
- [16] X. W. Din, F. Nunziata, X. F. Li, and M. Migliaccio, "Performance analysis and validation of waterline extraction approaches using single- and dual-polarization SAR data," *IEEE J. Sel. Topics Appl. Earth Obs. Remote Sens.*, vol. 8, no. 3, pp. 1019–1027, Mar. 2015.
- [17] T. Yu, S. Xu, X. Zhou, J. Xiao, and B. Zhang, "Semi-automatic extraction of the threshold segmentation of coastline based on coastline type," *IOP Conf. Ser. Earth Environ. Sci.*, vol. 690, pp. 12–19, 2021.
- [18] A. Spinosa, A. Ziemba, A. Saponieri, V. D. Navarro-Sanchez, L. Damiani, and G. E. Serafy, "Automatic extraction of shoreline from satellite images: A new approach," in *Proc. IEEE Int. Workshop Metrol. Sea; Learn. Measure Sea Health Parameters*, 2018, pp. 33–38.
- [19] A. Francone and D. J. Simmonds, "Assessing the reliability of a new one-line model for predicting shoreline evolution with impoundment field experiment data," *J. Mar. Sci. Eng.*, vol. 11, no. 5, 2023, Art. no. 1037.
- [20] O. Ronneberger, P. Fischer, and T. Brox, "U-net: Convolutional networks for biomedical image segmentation," in *Proc. Int. Conf. Med. Image Comput. Comput.-Assist. Interv.*, 2015, pp. 234–238.
- [21] S. Zhang, Q. Xu, H. Wang, Y. Kang, and X. Li, "Automatic waterline extraction and topographic mapping of tidal flats from SAR images based on deep learning," *Geophys. Res. Lett.*, vol. 49, no. 2, 2022, Art. no. e2021GL096007.
- [22] C. Xu et al., "SAR image water extraction using the attention U-net and multi-scale level set method: Flood monitoring in South China in 2020 as a test case," *Geospatial Inf. Sci.*, vol. 25, no. 2, pp. 155–168, 2022.
- [23] Y. Zhou et al., "Sea-land segmentation of Synthetic Aperture Radar imagery using deep neural network models," in *Proc. Photon. Electromagn. Res. Symp.*, 2021, pp. 2006–2010.
- [24] X. Chen, Q. Sun, and J. Hu, "Generation of complete SAR geometric distortion maps based on DEM and neighbor gradient algorithm," *Appl. Sci.*, vol. 8, no. 11, 2018, Art. no. 2206.
- [25] C. A. Baumhoer, A. J. Dietz, C. Kneisel, and C. Kuenzer, "Automated extraction of Antarctic Glacier and ice shelf fronts from Sentinel-1 imagery using deep learning," *Remote Sens.*, vol. 11, no. 21, 2019, Art. no. 2529.
- [26] K. Heidler, L. Mou, C. A. Baumhoer, A. J. Dietz, and X. X. Zhu, "HED-UNet: Combined segmentation and edge detection for monitoring the Antarctic coastline," *IEEE Trans. Geosci. Remote Sens.*, vol. 60, pp. 1–14, Mar. 2021, Art. no. 4300514.
- [27] A. Howard et al., "Searching for MobileNetV3," in *Proc. IEEE/CVF Int. Conf. Comput. Vis.*, 2019, pp. 1314–1324.
- [28] S. Woo, J. Park, J. Y. Lee, and I. S. Kweon, "CBAM: Convolutional block attention module," in *Proc. Eur. Conf. Comput. Vis.*, 2018, pp. 3–19.
- [29] L. Chang, Y. T. Chen, M. C. Wu, M. Alkhaleefah, and Y. L. Chang, "U-Net for Taiwan shoreline detection from SAR images," *Remote Sens.*, vol. 13, no. 20, 2022, Art. no. 5135.
- [30] J. S. Lee, "Refined filtering of image noise using local statistics," *Comput. Graph. Image Proc.*, vol. 15, no. 4, pp. 380–389, 1981.
- [31] E. H. Boak and I. L. Turner, "Shoreline definition and detection: A review," *J. Coast. Res.*, vol. 214, pp. 688–703, 2005.
- [32] T. M. Lillesand, R. W. Kiefer, and J. W. Chipman, *Remote Sensing and Image Interpretation*, 7th ed. Hoboken, NJ, USA: Wiley, 2015.
- [33] Nasa JPL, Pasadena, CA, USA, NASA Shuttle Radar topography Mission Global 3 arc second, NASA EOSDIS Land Processes DAAC, 2013, doi: [10.5067/MEASURES/SRTM/SRTMGL3.003](https://doi.org/10.5067/MEASURES/SRTM/SRTMGL3.003).
- [34] F. Bioresita and N. Hayati, "Coastline changes detection using Sentinel-1 satellite imagery in Surabaya, East Java, Indonesia," *J. Geod. Geomat.*, vol. 11, no. 2, pp. 190–198, 2016.
- [35] N. Kanopoulos, N. Vasanthavada, and R. L. Baker, "Design of an image edge detection filter using the Sobel operator," *IEEE J. Solid-State Circuits*, vol. 23, no. 2, pp. 358–367, Apr. 1988.
- [36] D. M. W. Powers, "Evaluation: From precision, recall and F-measure to ROC, informedness, markedness and correlation," *J. Mach. Learn. Technol.*, vol. 2, no. 1, pp. 37–63, 2011.
- [37] M. An, Q. Sun, J. Hu, Y. Tang, and Z. Zhu, "Coastline detection with Gaofen-3 SAR images using an improved FCM method," *Sensors*, vol. 18, no. 6, 2018, Art. no. 1898.
- [38] D. P. Kingma and J. Ba, "Adam: A method for stochastic optimization," in *Proc. 3rd Int. Conf. Learn. Representations*, 2015.
- [39] X. You and W. Li, "A sea-land segmentation scheme based on statistical model of sea," in *Proc. 4th Int. Congr. Image Signal Process.*, 2011, pp. 1155–1159.



Lena Chang (Member, IEEE) received the B.S. degree from National Tsing Hua University, Hsinchu, Taiwan, in 1985, the M.S. degree from the University of New Orleans, New Orleans, LA, USA, in 1987, and the Ph.D. degree from National Taiwan University, Taipei, Taiwan, in 1992, all in electrical engineering.

From 1987 to 1988, she worked as an Electrical Engineer with the Department of R&D, ADI Corp., Taipei. From 1992 to 2003, she was an Associate Professor with the Department of Merchant Marine, National Taiwan Ocean University, Keelung, Taiwan.

Since 2003, she has been an Associate Professor with the Department of Communications, Navigation and Control Engineering, National Taiwan Ocean University. Her research interests include the areas of remote sensing, computer vision, adaptive signal processing, and image processing.

Dr. Chang is a member of the Phi Tau Phi and Phi Kappa Phi Scholastic Honor Societies.



Yi-Ting Chen received the B.E. and M.S. degrees in 2018 and 2020, respectively, in communication, navigation and control engineering from National Taiwan Ocean University, Keelung, Taiwan, where he is currently working toward the Ph.D. degree in the Department of Electrical Engineering.

His research interests include remote sensing, image processing, deep learning, and computer vision.